

# An energy of asymmetry for accurate detection of global reflection axes

Dinggang Shen<sup>a</sup>, Horace H.S. Ip<sup>b,\*</sup>, Eam Khwang Teoh<sup>c</sup>

<sup>a</sup>Department of Radiology, Johns Hopkins University, Baltimore, MD 21287, USA

<sup>b</sup>Image Computing Group, Department of Computer Science, City University of Hong Kong, Kowloon, Hong Kong, People's Republic of China

<sup>c</sup>School of Electrical and Electronic Engineering, Nanyang Technological University, Singapore 639798, Singapore

Received 9 August 1999; revised 11 August 2000; accepted 4 September 2000

## Abstract

We define in this paper two energy terms, symmetric energy term and asymmetric energy term, which respectively correspond to the symmetric and asymmetric components of an object. The asymmetric energy term must be *zero*, if the studied object is invariant under a reflection about the  $x$ -axis. Accordingly, we formulate the problem of detecting reflectional symmetries as a problem of minimising the asymmetric energy term. From the local minima of the asymmetric energy term, we can detect *all* the symmetric axes of *any* object. Since the asymmetric energy term is expressed as a summation of a set of generalised complex (GC) moments computed for an object, the proposed symmetry detection method is robust against both noise and slight deformation. We use the steepest descent technique to calculate the local minima of the asymmetric energy term, whose initialisation is calculated from the most dominant GC moment. Experiments on typical logo images and human brain image have shown the effectiveness and the robustness of the proposed method. To our knowledge, this is the first theory on energy functions that describe the symmetric and asymmetric components of a 2D pattern. © 2001 Elsevier Science B.V. All rights reserved.

**Keywords:** Energy for symmetry and asymmetry; Reflectional symmetry; Symmetric axis; Generalised complex moments; Energy minimisation

## 1. Introduction

Reflectional symmetry is a very important type of symmetries in planar image and the presence of such cue helps in performing a wide variety of tasks such as guiding shape matching, model-based object matching and object recognition [1,2].

A straight line is an axis of symmetry of a planar object if the object is invariant under reflection about that line. Mirror symmetry is usually referred to an object with only *one* axis of symmetry. Generally, objects may have two or more axes of symmetries, denoted as *reflection-symmetric axes* in this paper. Various methods have been proposed to detect the reflection-symmetric axes of an object. However, the review given below shows that none of the previous methods are complete in the sense that they are unable to detect *all* reflection-symmetric axes of *any* object.

Previous methods were mainly focused on detecting *one* single reflection-symmetric axis. Labonte et al. [3] studied the problem of detecting global *bilateral* symmetry in images consisting of dense arrangements of local features,

such as dots or oriented segments. Zielke et al. [4] only looked at vertical or near-vertical symmetry axes in an image for car-following.

Other methods attempted to detect *two or more* reflection-symmetric axes. Atallah [5] detected the axes of reflectional symmetries by first determining the centroid position and then using a string pattern matching technique, which considered all possible lines passing through the centroid. However, the main drawback is that this method is only applicable to planar figures made up of (possibly intersecting) segments, circles, points, etc. Marloa [6] presented an algorithm for finding the number and positions of the symmetry axes of a symmetric or almost-symmetric planar object, while this technique required the evaluation of some rational functions. Masuda et al. [7] presented a method to detect reflectional symmetry by performing correlation with the reflected images. But the disadvantage with this method is high computational cost and memory requirement, since all possible transformations have to be tested. Sun and Sherrah [8] formulated the symmetry detection problem as a correlation of the Gaussian image. As stated in the paper, their technique determines the symmetric axis assuming a priori that the input image is symmetric. However, this technique cannot be used to determine whether the input image is symmetric or not.

\* Corresponding author. Tel.: +852-2788-8641; fax: 852-2788-8614.

E-mail addresses: dgshen@cbmv.jhu.edu (D. Shen), cship@cityu.edu.hk (H.H.S. Ip), eekteoh@ntu.edu.sg (E.K. Teoh).

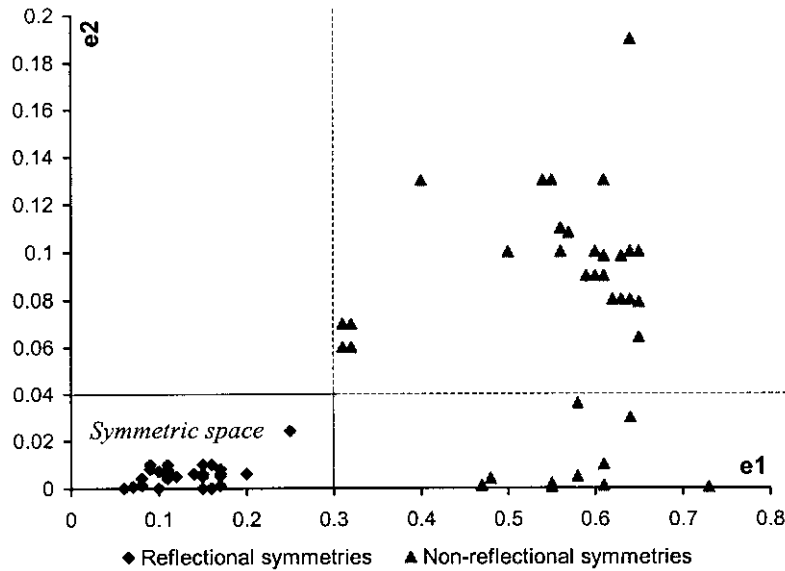


Fig. 1. A training set with reflectional symmetries and non-reflectional symmetries for estimating the values of two thresholds  $\epsilon_1$  and  $\epsilon_2$ .

A spectral-based method has been designed for detecting the centre of a *quasi*-symmetrical object [9]. The disadvantage of this method is that it can only be applied to *quasi*-symmetrical objects, not any type of symmetrical objects.

In this paper, we present a new formulation of the symmetry detection problem in terms of energy minimisation. The advantage of this formulation is that all the global reflection-symmetric axes can be detected accurately. We define a novel energy function based on a set of Generalised Complex (GC) moments [10,11] computed for an object. This novel energy function can be separated into two terms, symmetric energy term and asymmetric energy term, which, respectively, correspond to the symmetric and the asymmetric components of the object. We proved that *the asymmetric energy term must be zero*, if the studied object is invariant under a reflection about the  $x$ -axis. That means, we can compute the orientations of the reflectional axes by searching the orientations that make the asymmetric energy term zero. However, in real application the asymmetric energy term might not be exactly zero at those orientations, since the studied symmetric object might be corrupted by noise or even imperfectly symmetric. This way, we calculate a set of orientations that make the asymmetric energy term minimal, and from this set of orientations we screen out the false orientations and obtain the reflection-symmetric orientations. The local minima of the asymmetric energy term are calculated by the steepest descent technique, whose initialisation is determined by a GC moment with the largest magnitude. The two constraints are proposed to screen out the false orientations.

This paper is organised as follows. The properties of GC moments of the reflection-symmetric object are described in Section 2. In particular, *we show that the asymmetric energy term must be zero for the object invariant under a reflection about the  $x$ -axis*. Based on these properties, Section 3

proposes a method of detecting reflectional symmetries. Two constraints for screening out false symmetry angles are also given in the same section. Experiments on typical logo images and human brain image are provided in Section 4 for demonstrating the performance of our method. Section 5 gives the conclusions.

## 2. Properties of reflection-symmetric object

Generalised complex (GC) moments are used here as a set of global features for detecting the reflection-symmetric axes of an object. In this section, we analyse the properties related to the GC moments of the reflection-symmetric object (Theorem 1) and show that the asymmetric energy term goes to zero for the object with  $x$ -axis as its reflectional axis (Theorem 2).

The definition of a GC moment for any image object is given in Definition 1, where  $f(r, \theta)$  is a function of a centred image object in the polar coordinate.

**Definition 1.** The  $pq$ -order GC moment of the image function  $f(r, \theta)$  is defined as:

$$GC_{p,q} = R_{p,q} e^{j\varphi_{p,q}} = \frac{1}{2\pi} \int_0^{2\pi} \int_0^{\infty} f(r, \theta) (r^p e^{jq\theta}) r dr d\theta,$$

where  $p$  is a non-negative integer and  $q$  a positive integer.

An image is said to be reflection-symmetric, if it is invariant to reflection with respect to one or more straight lines. Notice that we have made image centred, that is, the origin coincides with the geometric centre of mass of the image. It can be proven that these symmetric axes pass through the centre of mass of the image. Mathematically,

the reflection-symmetric object satisfies:

$$f(r, \phi + \theta) = f(r, \phi - \theta),$$

where  $\phi$  is an angle from the  $x$ -axis to the symmetric axis. Note that this mathematical form is also a necessary and sufficient condition for an object  $f(r, \theta)$  to be reflection-symmetric about the  $x$ -axis [12].

Before using the GC moments to detect all the reflection-symmetric axes of an object, we need to establish the properties associated with the GC moments of the reflection-symmetric object. Theorem 1 describes one particular form of these properties: if all the detected GC moments are real, then the object  $f(r, \theta)$  is reflection-symmetric about the  $x$ -axis.

**Theorem 1.** All GC moments  $GC_{p,q}$  are real, if the input image object  $f(r, \theta)$  is invariant under a reflection about the  $x$ -axis.

**Proof.** Since the  $x$ -axis is a reflection-symmetric axis of an object  $f(r, \theta)$ , we have  $f(r, \theta) = f(r, -\theta)$ . Accordingly, we can simplify  $GC_{p,q}$  as follows:

$$\begin{aligned} GC_{p,q} &= \frac{1}{2\pi} \int_0^{2\pi} \int_0^\infty f(r, \theta)(r^p e^{jq\theta})r \, dr \, d\theta \\ &= \frac{1}{2\pi} \int_0^\pi \int_0^\infty f(r, \theta)(r^p e^{jq\theta})r \, dr \, d\theta \\ &\quad + \frac{1}{2\pi} \int_\pi^{2\pi} \int_0^\infty f(r, \theta)(r^p e^{jq\theta})r \, dr \, d\theta \\ &= \frac{1}{2\pi} \int_0^\pi \int_0^\infty f(r, -\theta)(r^p e^{jq\theta})r \, dr \, d\theta \\ &\quad + \frac{1}{2\pi} \int_{-\pi}^0 \int_0^\infty f(r, \theta)(r^p e^{jq\theta})r \, dr \, d\theta \\ &= -\frac{1}{2\pi} \int_0^{-\pi} \int_0^\infty f(r, \theta)(r^p e^{-jq\theta})r \, dr \, d\theta \\ &\quad + \frac{1}{2\pi} \int_{-\pi}^0 \int_0^\infty f(r, \theta)(r^p e^{jq\theta})r \, dr \, d\theta \\ &= \frac{1}{2\pi} \int_{-\pi}^0 \int_0^\infty f(r, \theta)r^p (e^{-jq\theta} + e^{jq\theta})r \, dr \, d\theta \\ &= \frac{1}{2\pi} \int_{-\pi}^0 \int_0^\infty f(r, \theta)r^p 2 \cos(q\theta)r \, dr \, d\theta. \end{aligned}$$

It can be concluded from the above expressions that  $GC_{p,q}$  is real, if  $f(r, \theta)$  is reflection-symmetric about the  $x$ -axis.  $\square$

In practice, it may not be possible for us to first calculate all the GC moments and then determine the reflection-symmetric axes of an object based on all the calculated GC moments. In fact, the order  $p$  in  $GC_{p,q}$  is usually fixed at a particular value  $P$  when the GC moments are used for detecting the reflection axes [10,11]. If we use only  $N$  GC

moments, i.e.  $\{GC_{P,q} | 0 \leq q \leq (N - 1)\}$ , to detect the reflection-symmetric axes, then we can define the total energy contained in these  $N$  GC moments as:

$$E_{\text{Total}} = 2\pi \sum_{q=0}^{N-1} \|GC_{P,q}\|^2 = 2\pi \sum_{q=0}^{N-1} R_{P,q}^2.$$

More interestingly, we can divide this energy function into two terms that express the energy associated with the symmetric and asymmetric components of the object. That is,

$$\begin{aligned} E_{\text{Total}} &= 2\pi \sum_{q=0}^{N-1} \{(R_{P,q} \cos(\varphi_{P,q}))^2 + (R_{P,q} \sin(\varphi_{P,q}))^2\} \\ &= E_{\text{Sym}} + E_{\text{Asym}}, \end{aligned}$$

where

$$E_{\text{Sym}} = 2\pi \sum_{q=0}^{N-1} (R_{P,q} \cos(\varphi_{P,q}))^2 \quad \text{and}$$

$$E_{\text{Asym}} = 2\pi \sum_{q=0}^{N-1} (R_{P,q} \sin(\varphi_{P,q}))^2.$$

From the definitions of  $E_{\text{Sym}}$  and  $E_{\text{Asym}}$  and the proof of Theorem 1, we can observe that  $E_{\text{Sym}}$  is a symmetric energy term corresponding to the symmetric component of the object and  $E_{\text{Asym}}$  is an asymmetric energy term corresponding to the asymmetric component of the object.

From the proof of Theorem 1, it is easy to prove Theorem 2. Obviously, in this case the total energy is equal to the symmetric energy term, i.e.  $E_{\text{Total}} = E_{\text{Sym}}$ . To our knowledge, this is the first proof of an energy function that makes explicit the energy of a 2D pattern due to its symmetric and asymmetric components and hence enables us to formulate symmetry detection as an energy minimisation problem.

**Theorem 2.** The asymmetric energy term is zero, i.e.

$$E_{\text{Asym}} = 2\pi \sum_{q=0}^{N-1} (R_{P,q} \sin(\varphi_{P,q}))^2 = 0,$$

if an object  $f(r, \theta)$  is invariant under a reflection about  $x$ -axis.

Given these two theorems, we then derive an energy-based reflection symmetry detection algorithm in Section 3.

### 3. Reflection-symmetry detection by minimising the asymmetry energy term

In this section, we describe a process to solve the two central problems: (1) whether an object  $f(r, \theta)$  is reflection-symmetric or not, and (2) the location of all the reflection-symmetric axes. It should be noted that as shown in Section 1, most previous

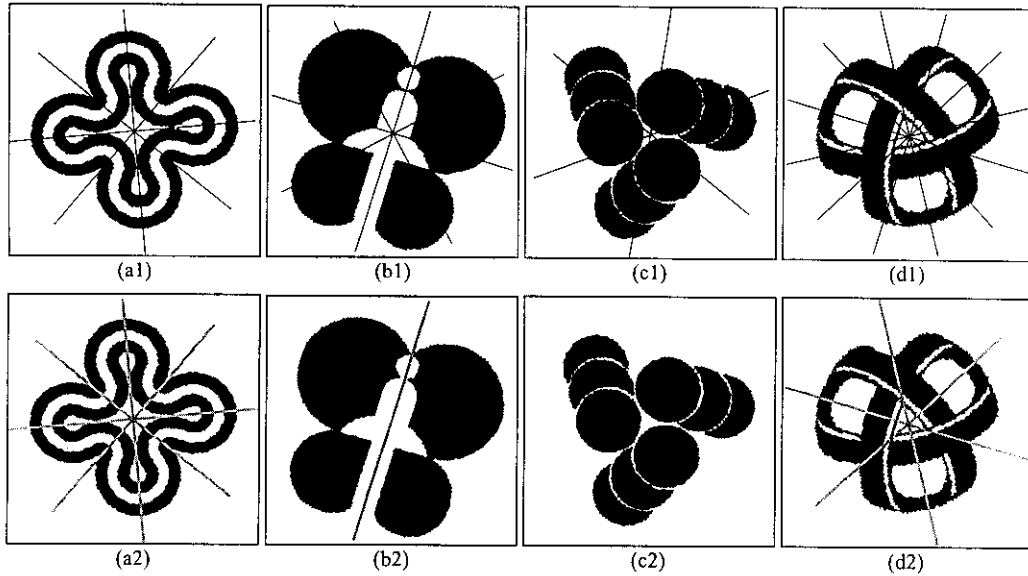


Fig. 2. Reflection symmetries detection on four noise-free logo images. In (a1)–(d1), the axes are determined by only the most dominant GC moment  $GC_{P,Q}$ . In (a2)–(d2), the reflection symmetries are determined by our energy-based method which considering all the  $N$  GC moments.

techniques assume that problem (1) is known and focus on solving (2). However, in general, problem (1) is usually not known a priori and its solution is not trivial. Our contribution in this paper is that these two fundamental problems can be jointly solved by only analysing the asymmetry energy term.

Even an image object is reflection-symmetric, because of rotation its reflection-symmetric axis is not necessarily localised on the  $x$ -axis. In the following, we will analyse the variation of the asymmetry energy term with respect to the rotation angle  $\alpha$  of the reflection-symmetric axis.

Let the image object  $f(r, \theta)$  be counter-clockwise rotated

by an angle of  $\alpha$ , and become  $f(r, \theta - \alpha)$ . Then the corresponding GC moments of the rotated image object  $f(r, \theta - \alpha)$  become  $GC_{P,q} e^{jq\alpha}$ . Similarly, the asymmetric energy term  $E_{Asym}^\alpha$  of the rotated image object  $f(r, \theta - \alpha)$  becomes

$$E_{Asym}^\alpha = 2\pi \sum_{q=0}^{N-1} (R_{P,q} \sin(\varphi_{P,q} + q\alpha))^2.$$

If the rotation angle  $\alpha$  is zero, then  $E_{Asym}^0 = E_{Asym}$  because of  $f(r, \theta - 0) = f(r, \theta)$ . Hence, the problems of determining (a) whether an object is reflection-symmetric and (b) the

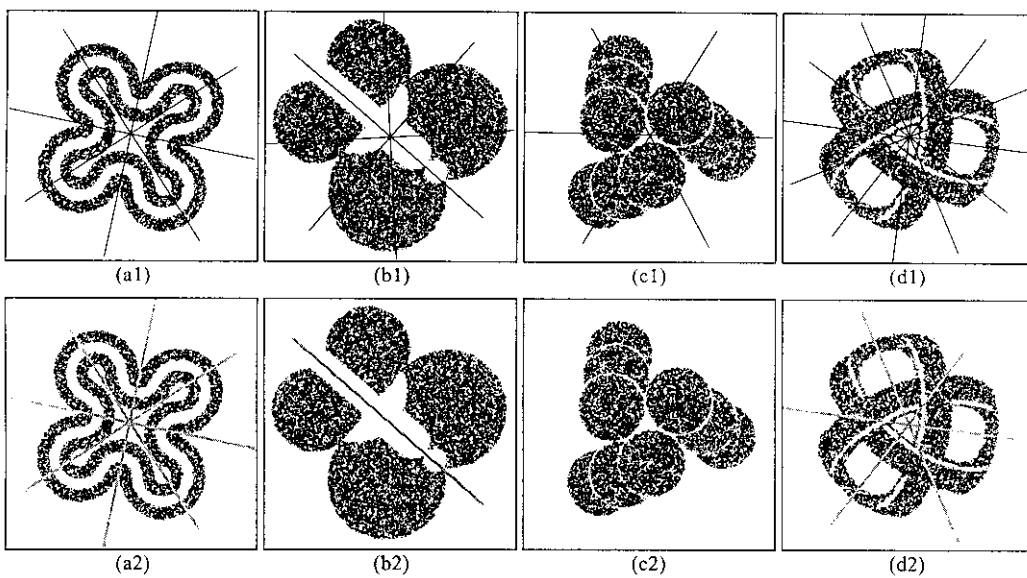


Fig. 3. Reflection symmetries detection on four noise-corrupted image objects, which are identical to objects in Fig. 2. Refer to Fig. 2 for the meanings of each subfigure.

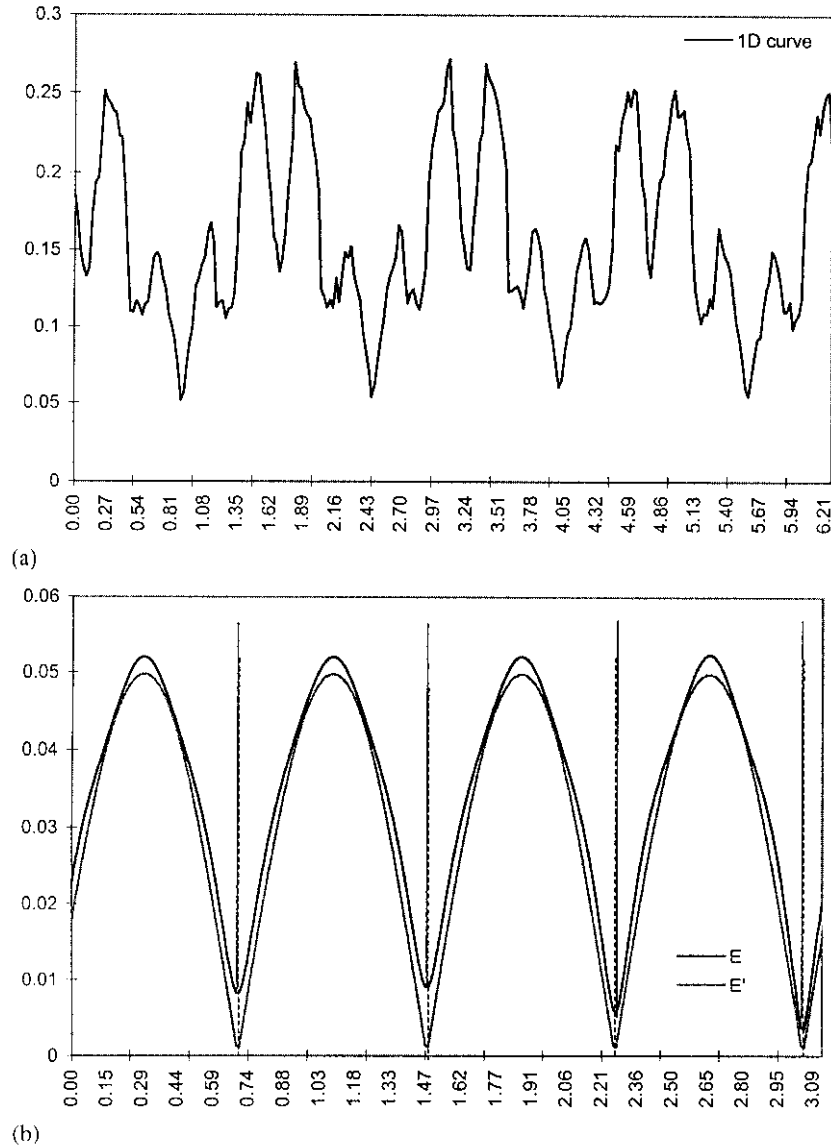


Fig. 4. (a) 1D radial projection of the image function (in Fig. 2(a)) or  $r^0$ , and (b) the local minima of the asymmetric energy term  $E = E_{\text{Asym}}^\alpha$ . Here  $E^l = 2\pi(R_{0,4} \sin(\varphi_{0,4} + 4\alpha))^2$ . Solid vertical lines denote the converged angles, while dotted vertical lines denote the initial angles.

locations of all its reflection-symmetric axes become the problem of finding the angle set  $\{\alpha_i | 1 \leq i \leq M\}$  which makes  $E_{\text{Asym}}^{\alpha_i}$  equal to zero, i.e.  $E_{\text{Asym}}^{\alpha_i} = 0$ . If the number  $M$  is *not* equal to zero, then the object  $f(r, \theta)$  has  $M$  reflection-symmetric axes that pass through the origin at the angles  $\{-\alpha_i | 1 \leq i \leq M\}$ . (Notice that the angles for the reflection-symmetric axes of the object are  $-\alpha_i$ , not  $\alpha_i$ .) On the other hand, if  $M = 0$ , then the object is *not* reflection-symmetric.

Owing to the facts that noise exists in real applications and also the object might not be perfectly reflection-symmetric, there may exist no angle  $\alpha$  making  $E_{\text{Asym}}^\alpha$  exactly zero. Therefore, in practice, we *first* calculate the angles  $\{\alpha_i\}$  that make  $E_{\text{Asym}}^\alpha$  local minima, and *then* use additional constraints to validate whether the axes that

pass through the origin at angles  $\{-\alpha_i\}$  are indeed the true reflection-symmetric axes.

We observe that analytic solutions may not exist for directly computing the local minima of  $E_{\text{Asym}}^\alpha$ , due to the complicated mathematical form of  $E_{\text{Asym}}^\alpha$ . Instead, these local minima can be located using the steepest descent technique. Initialisation in the steepest descent technique is usually the most important and difficult part. We address the initialisation issue in the following.

We first analyse the asymmetric energy term  $E_{\text{Asym}}^\alpha$ , and then choose the set of initial angles. For convenience,  $E_{\text{Asym}}^\alpha$  is rewritten as follows:

$$E_{\text{Asym}}^\alpha = 2\pi \sum_{q=0}^{N-1} (R_{P,q} \sin(\varphi_{P,q} + q\alpha))^2.$$

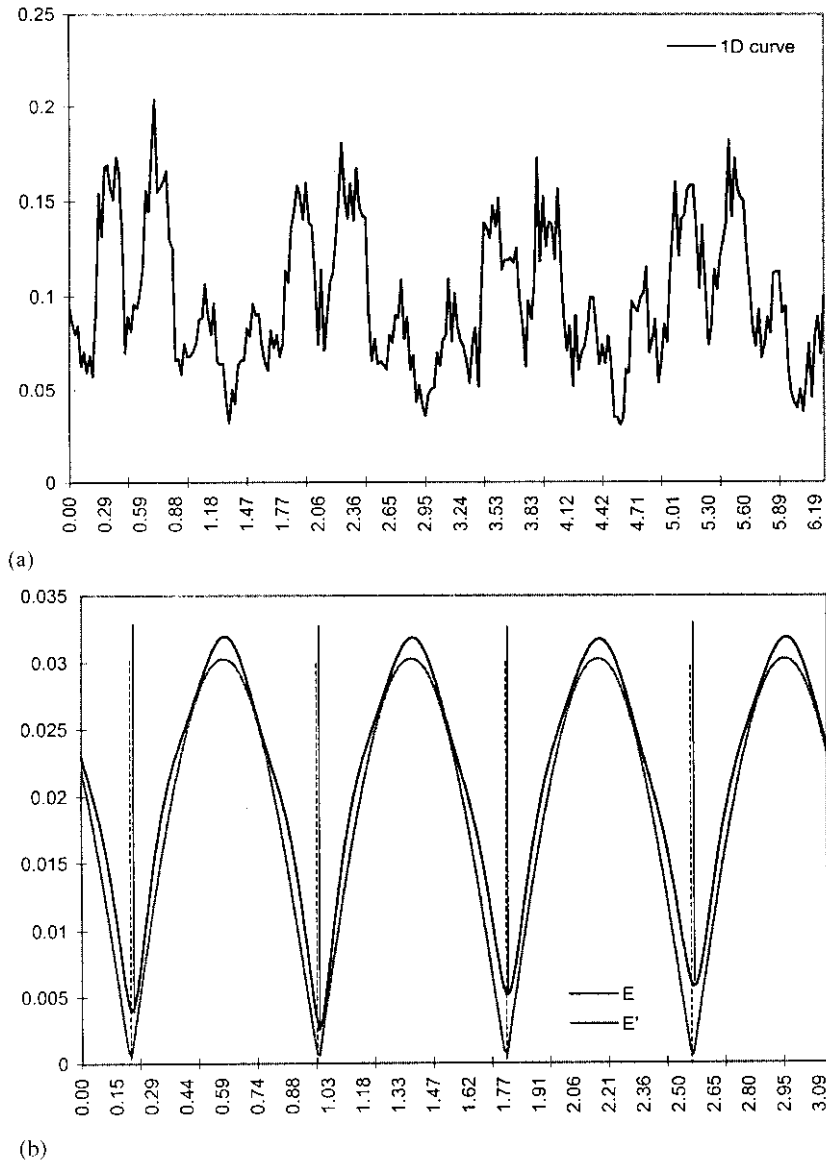


Fig. 5. (a) 1D radial projection of the *noisy* image function (in Fig. 3(a)) on  $r^0$ , and (b) the local minima of the asymmetric energy term  $E = E_{Asym}^\alpha$ . Here  $E' = 2\pi(R_{0,4} \sin(\varphi_{0,4} + 4\alpha))^2$ . Solid vertical lines denote the converged angles, while dotted vertical lines denote the initial angles.

Let us assume that  $R_{P,Q}$ , where  $0 \leq Q \leq (N - 1)$ , be the largest value in the set of all  $N$  magnitudes  $\{R_{P,q} | 0 \leq q \leq (N - 1)\}$ . Therefore, we can say that, the term  $2\pi(R_{P,Q} \sin(\varphi_{P,Q} + Q\alpha))^2$  in  $E_{Asym}^\alpha$  is the dominant term affecting the value of  $E_{Asym}^\alpha$ . Also, the *potential* local minima should be near to the angles that make this dominant term  $2\pi(R_{P,Q} \sin(\varphi_{P,Q} + Q\alpha))^2$  zero. We can easily compute the angles satisfying the requirement,  $2\pi(R_{P,Q} \sin(\varphi_{P,Q} + Q\alpha))^2 = 0$ , i.e.

$$\alpha_i = -\frac{\varphi_{P,Q} + i\pi}{Q}, \quad i = 0, 1, \dots, (Q - 1).$$

Thus the evaluated angle can be used as the initial variables  $\alpha_i^{(0)} = \alpha_i$  for the steepest descent technique. A more

accurate (or refined) angle can be obtained by the following iteration equation:

$$\alpha_i^{(t+1)} = \alpha_i^{(t)} - \eta \frac{\partial E_{Asym}^\alpha}{\partial \alpha} \Big|_{\alpha=\alpha_i^{(t)}}, \quad i = 0, 1, \dots, (Q - 1),$$

where  $\eta$  is the learning rate and  $\partial E_{Asym}^\alpha / \partial \alpha$  is the derivative with respect to  $\alpha$ , in detail:

$$\frac{\partial E_{Asym}^\alpha}{\partial \alpha} = 2\pi \sum_{q=0}^{N-1} (R_{P,q})^2 \sin(2\varphi_{P,q} + 2q\alpha)q.$$

After convergence, we can obtain  $Q$  final angles  $\{\alpha_i^{(T_i)}\}$ , where  $T_i$  is the number of iterations needed to make  $\alpha_i^{(t)}$  converged. However, not all such converged angles

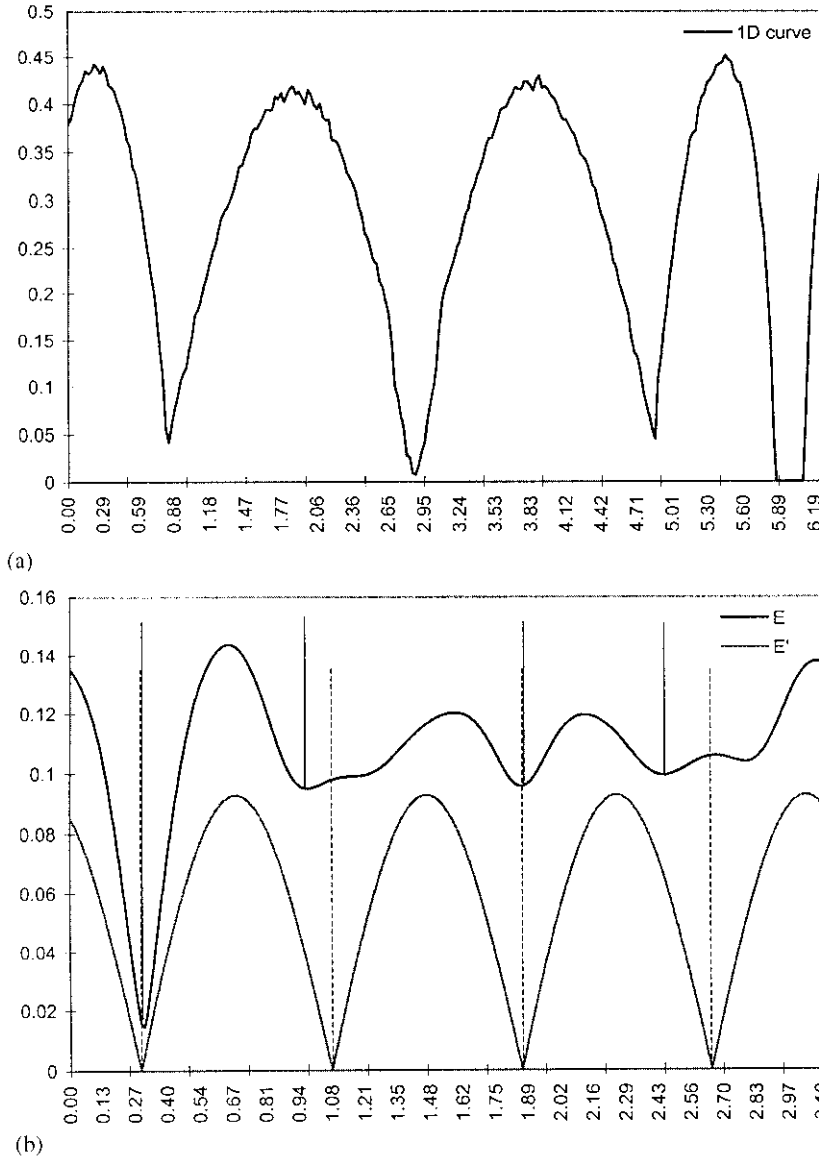


Fig. 6. (a) 1D radial projection of the image function (in Fig. 2(b)) on  $r^0$ , and (b) the local minima of the asymmetric energy term  $E = E^{\alpha}_{Asym}$ . Here  $E' = 2\pi(R_{0,4} \sin(\varphi_{0,4} + 4\alpha))^2$ . Solid vertical lines denote the converged angles, while dotted vertical lines denote the initial angles.

necessarily correspond to the reflection-symmetric axes of the object. We thus design two additional constraints to select the true ones from the set of converged angles  $\{\alpha_i^{(T_i)}\}$ . The two constraints used here are:

$$(a) \quad \frac{E^{\alpha}_{Asym}}{E_{Total}} \Big|_{\alpha=\alpha_i^{T_i}} \leq \varepsilon_1,$$

$$(b) \quad \|\alpha_i^{(T_i)} - \alpha_i^{(0)}\| \leq \varepsilon_2.$$

The constraint (a) means that  $E^{\alpha}_{Asym}|_{\alpha=\alpha_i^{T_i}}$  should only be a small portion of the total energy  $E_{Total}$ , since Theorem 2 requires that the asymmetric energy term be zero for any reflection-symmetric object. Constraint (b) indicates that the

converged angle  $\alpha_i^{(T_i)}$  should be very close to the initial angle  $\alpha_i^{(0)}$ . Otherwise, the term  $2\pi(R_{P,Q} \sin(\varphi_{P,Q} + Q\alpha))^2|_{\alpha=\alpha_i^{T_i}}$  will become large and  $E^{\alpha}_{Asym}|_{\alpha=\alpha_i^{T_i}}$  will be large too.

The values of two thresholds  $\varepsilon_1$  and  $\varepsilon_2$  used above can be determined automatically by a training set. For example, there are totally 28 reflectional symmetries and 43 non-reflectional symmetries in our training set. Let us define parameters  $e1$  and  $e2$  as  $e1 = E^{\alpha}_{Asym}/E_{Total}|_{\alpha=\alpha_i^{T_i}}$  and  $e2 = \|\alpha_i^{(T_i)} - \alpha_i^{(0)}\|$ . In Fig. 1, the horizontal axis denotes parameter  $e1$  and the vertical axis denotes parameter  $e2$ . The symbols “♦” represent the values of parameters  $(e1, e2)$  calculated from the reflectional symmetries, while the symbols “Δ” denote the values of parameters  $(e1, e2)$

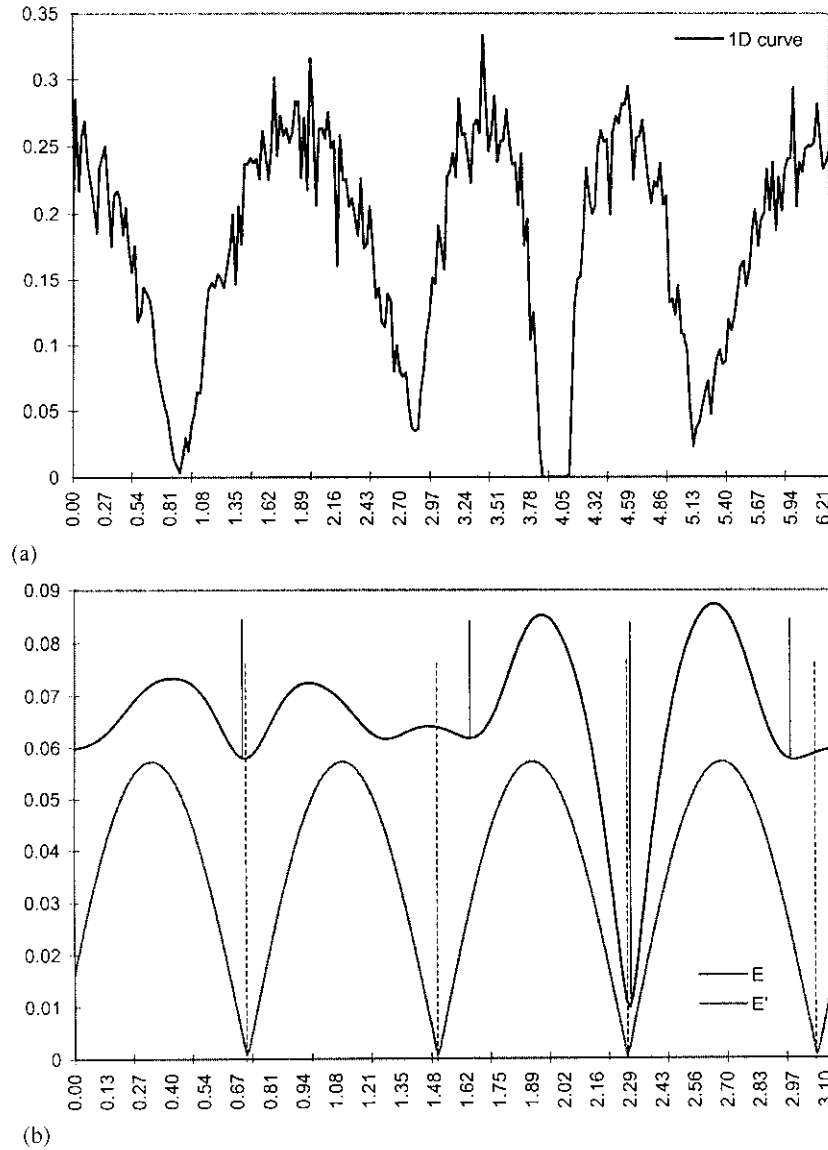


Fig. 7. (a) 1D radial projection of the *noisy* image function (in Fig. 3(b)) on  $r^0$ , and (b) the local minima of the asymmetric energy term  $E = E_{Asym}^\alpha$ . Here  $E' = 2\pi(R_{0,4} \sin(\varphi_{0,4} + 4\alpha))^2$ . Solid vertical lines denote the converged angles, while dotted vertical lines denote the initial angles.

calculated from the non-reflectional symmetries. In order to correctly discriminate reflectional symmetries from non-reflectional symmetries, here the values of two thresholds  $\varepsilon_1$  and  $\varepsilon_2$  are roughly chosen as  $\varepsilon_1 = 0.3$  and  $\varepsilon_2 = 0.04$ . The thin lines in Fig. 1 clearly denote these thresholds. For reflectional symmetry, its parameters ( $e1, e2$ ) are supposed to be localised in the space that is enclosed by two thin solid lines and two axes. In Section 4, we use these two chosen thresholds to automatically detect reflectional symmetries in the tested images.

The final algorithm for detecting reflection-symmetric axes of the object using the energy-based method is summarised as follows:

1. Using a fixed order  $p = P$ , calculate the first  $N$  GC

moments of an image object, i.e.  $\{GC_{P,q} | 0 \leq q \leq (N - 1)\}$ .

2. Select the largest magnitude  $R_{P,Q}$ , where  $0 \leq Q \leq (N - 1)$ , from the set of the  $N$  magnitudes  $\{R_{P,q} | 0 \leq q \leq (N - 1)\}$ .
3. Obtain the angles that satisfy the equation  $2\pi(R_{P,Q} \sin(\varphi_{P,Q} + Q\alpha))^2 = 0$ , that is

$$\alpha_i = -\frac{\varphi_{P,Q} + i\pi}{Q}, \quad i = 0, 1, \dots, (Q - 1).$$

4. Regard the angles  $\alpha_i$   $i = 0, 1, \dots, (Q - 1)$ , as the initial variables and use the steepest descent technique to achieve

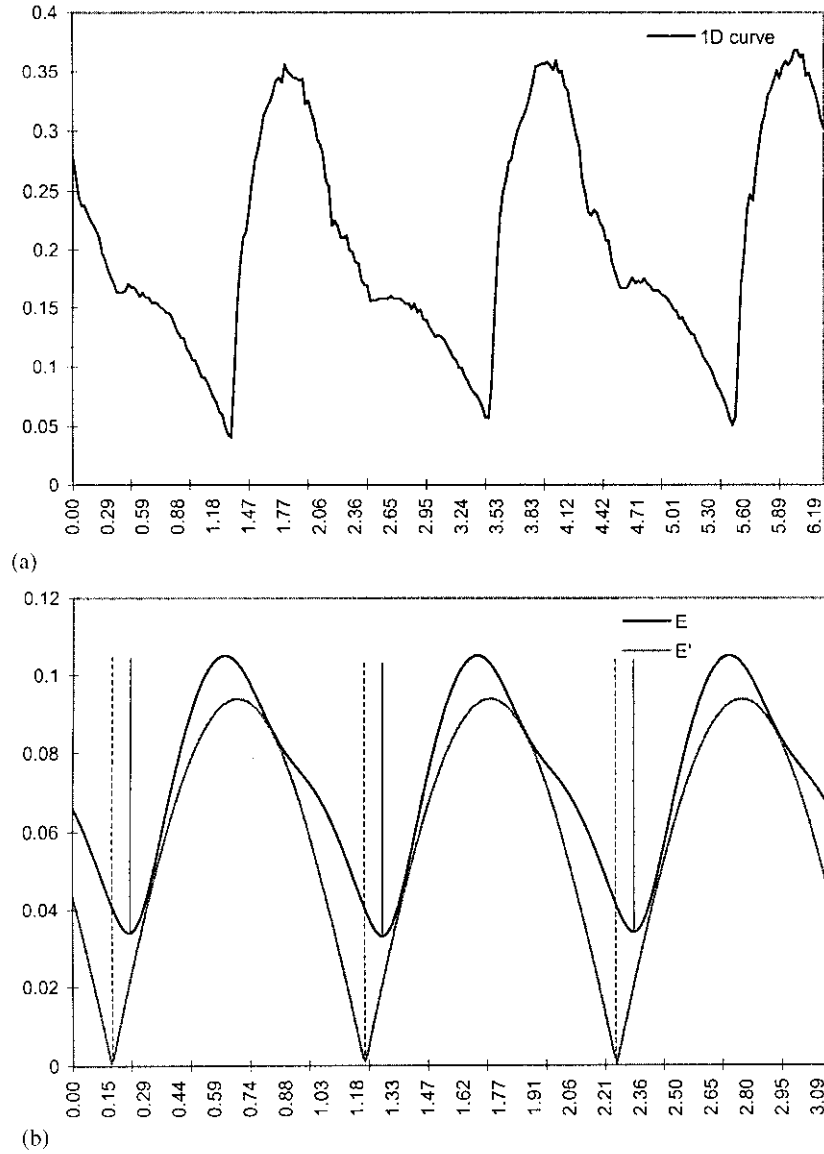


Fig. 8. (a) 1D radial projection of the image function (in Fig. 2(c)) on  $r^0$ , and (b) the local minima of the asymmetric energy term  $E = E_{Asym}^\alpha$ . Here  $E^l = 2\pi(R_{0,3} \sin(\varphi_{0,3} + 3\alpha))^2$ . Solid vertical lines denote the converged angles, while dotted vertical lines denote the initial angles.

the converged variables. The iteration equation is

$$\alpha_i^{(t+1)} = \alpha_i^{(t)} - \eta \left. \frac{\partial E_{Asym}^\alpha}{\partial \alpha} \right|_{\alpha=\alpha_i^{(t)}}, \quad i = 0, 1, \dots, (Q - 1),$$

where

$$\frac{\partial E_{Asym}^\alpha}{\partial \alpha} = 2\pi \sum_{q=0}^{N-1} (R_{P,q})^2 \sin(2\varphi_{P,q} + 2q\alpha)q.$$

5. Apply the two constraints to validate the true reflection-symmetric angles from the set of the converged angles. These two constraints are: (a)  $E_{Asym}^\alpha / E_{Total} |_{\alpha=\alpha_i^{(T)}} \leq \varepsilon_1$  and (b)  $\|\alpha_i^{(T_i)} - \alpha_i^{(0)}\| \leq \varepsilon_2$ .

6. The *real* reflection-symmetric axes are those which pass through the origin at angles  $-\alpha_i^{(T_i)}$  and satisfy the two constraints in Step (5).

#### 4. Experiments on detecting reflectional symmetries

In this section, we demonstrate the performance of our method in detecting the reflection symmetries. The experimental results show that all the reflectional symmetries of *every* image in our image database can be successfully detected. Notice that there are over 200 image patterns in our image database. In the following, Sections 4.1 and 4.2 demonstrate the performances of our method in detecting

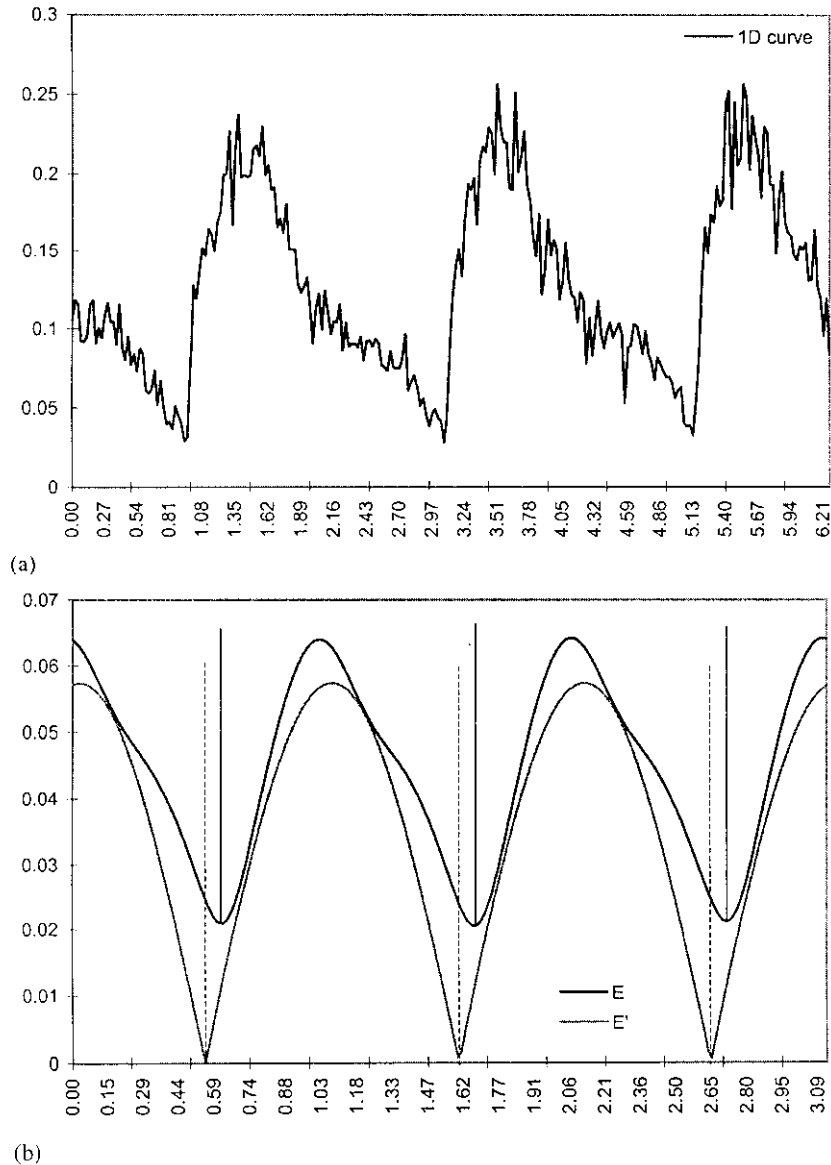


Fig. 9. (a) 1D radial projection of the *noisy* image function (in Fig. 3(c)) on  $r^0$ , and (b) the local minima of the asymmetric energy term  $E = E_{Asym}^\alpha$ . Here  $E' = 2\pi(R_{0,3} \sin(\varphi_{0,3} + 3\alpha))^2$ . Solid vertical lines denote the converged angles, while dotted vertical lines denote the initial angles.

reflectional symmetries of the images of logos and real objects. Section 4.3 evaluates the sensitivity of our method to the errors of locating the geometric centre of the image.

#### 4.1. Logo images

To clearly demonstrate the ability and procedure of our energy-based method, four objects and their noisy versions, respectively, shown in Figs. 2 and 3, are used as examples in this paper. Grey thick lines in Figs. 2 and 3 denote the detected reflection-symmetric axes using our method, while the black thin lines represent the potential axes that are calculated by using only a GC moment with the largest magnitude.

For the *first* image shown in Figs. 2(a) and 3(a), the

number of the reflection-symmetric axes as determined by its most dominant GC moment  $GC_{0,4}$  are the same as the ones determined by our energy-based method that considers all  $N$  GC moments. In our experiments,  $N$  is chosen to be 15, and  $P = 0$  in  $GC_{P,q}$ . Readers can refer to Ref. [10] for the criteria of selecting the appropriate value for the parameter  $p$  in  $GC_{p,q}$ . For the *second* image shown in Figs. 2(b) and 3(b), the true number of reflection-symmetric axes is less than that determined by the most dominant GC moment ( $GC_{0,4}$ ) of this image. For the *third* image in Figs. 2(c) and 3(c), our method correctly detects that no real reflection-symmetric axis actually exists. But, three false axes were determined by the image's most dominant GC moment  $GC_{0,3}$ . Actually, the *fourth* object in Figs. 2(d) and 3(d) is not perfectly reflection-symmetric. However, since GC moments are

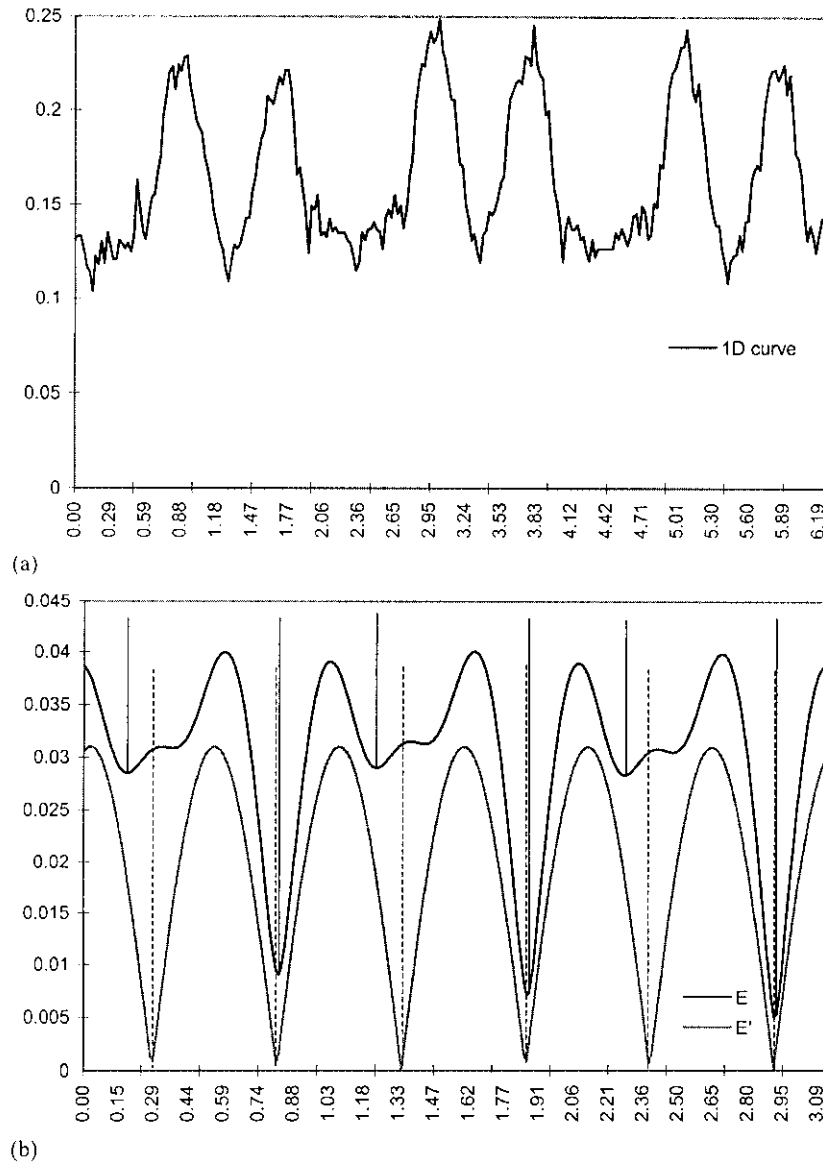


Fig. 10. (a) 1D radial projection of the image function (in Fig. 2(d)) on  $r^0$ , and (b) the local minima of the asymmetric energy term  $E = E_{\text{Asym}}^\alpha$ . Here  $E' = 2\pi(R_{0,6} \sin(\varphi_{0,6} + 6\alpha))^2$ . Solid vertical lines denote the converged angles, while dotted vertical lines denote the initial angles.

global features of the object and all  $N$  GC moments are combined together into a single asymmetric energy term  $E_{\text{Asym}}^\alpha$ , our method is able to detect those imperfect (but perceptually) reflectional symmetries.

In Figs. 4–11, subfigure (a) is the 1D radial projection of the image function  $f(r, \theta)$  on  $r^0$  (notice  $P = 0$ ). Obviously, the reflection-symmetric property of the 2D image is also preserved in its 1D radial projection. That means, the detection of reflection-symmetries of the 2D image can be completed by analysing its 1D radial projection. In subfigure (b), the black curve represents the asymmetric energy term  $E_{\text{Asym}}^\alpha$  in the domain  $0 \leq \alpha \leq \pi$ , while the grey curve represents the variation of the particular term  $2\pi(R_{P,Q} \sin(\varphi_{P,Q} + Q\alpha))^2$  with the angle  $\alpha$ . The dotted vertical lines in subfigure (b) represent the initial angles as

calculated from the most dominant GC moment of the object, while the solid vertical lines represent the final converged angles.

*Experiments on the first image object shown in Figs. 2(a) and 3(a).* In all  $N = 15$  GC moments of this object (Fig. 2(a)), the magnitude of  $\text{GC}_{0,4}$  is the largest one. The reflection-symmetric axes determined by using only  $\text{GC}_{0,4}$  are shown in Fig. 2(a1). The corresponding angles  $\alpha_i$ , the initial angles  $\alpha_i^{(0)}$ , and finally converged angles  $\alpha_i^{(T_i)}$  are shown in Table 1. Here  $i = 0, 1, \dots, 3$ . In Fig. 4(b), the grey curve represents the variation of the term  $E' = 2\pi(R_{0,4} \sin(\varphi_{0,4} + 4\alpha))^2$  with the angle  $\alpha$ , and the dotted vertical lines represent the initial angles that are calculated from  $\text{GC}_{0,4}$ . Only one iteration step is needed to locate all the local minima. After applying the two constraints, we found

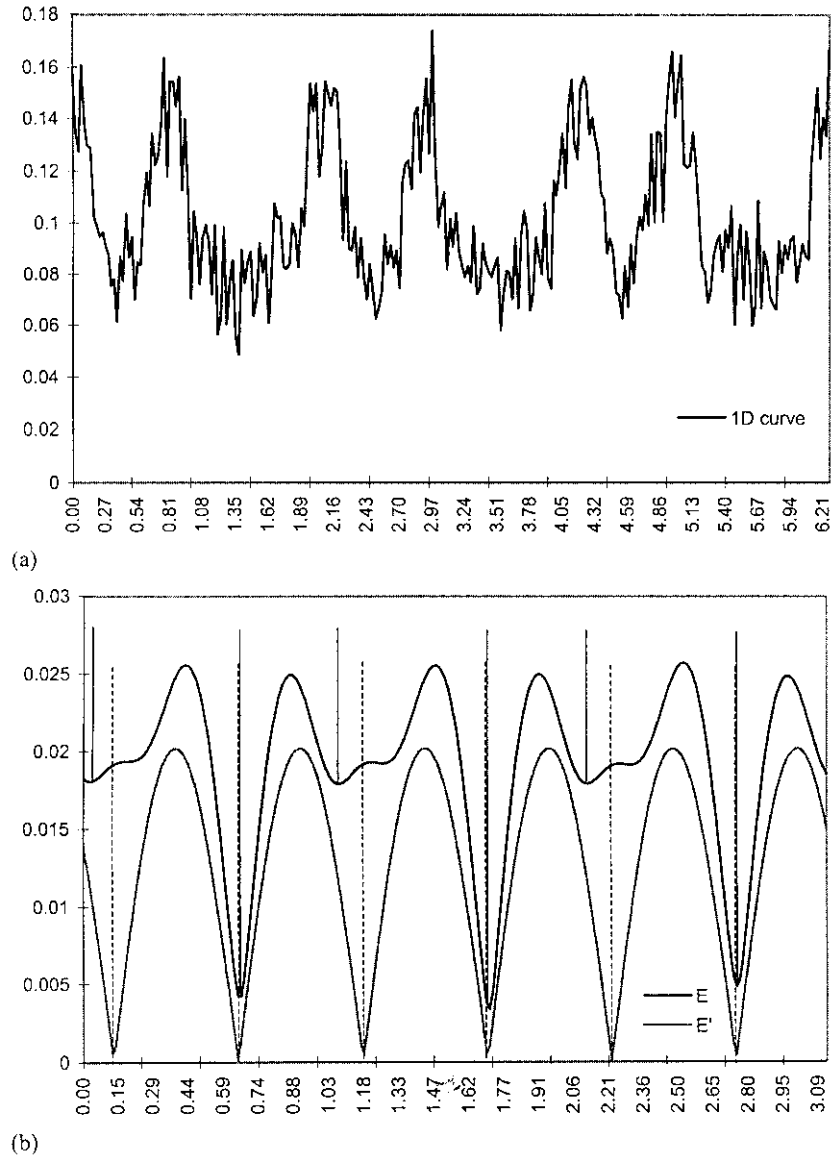


Fig. 11. (a) 1D radial projection of the *noisy* image function (in Fig. 3(d)) on  $r^0$ , and (b) the local minima of the asymmetric energy term  $E = E_{Asym}^\alpha$ . Here  $E' = 2\pi(R_{0,6} \sin(\varphi_{0,6} + 6\alpha))^2$ . Solid vertical lines denote the converged angles, while dotted vertical lines denote the initial angles.

Table 1  
Angles calculated for the first object in Fig. 2(a) ( $GC_{P,Q} = GC_{0,4} = 0.1863e^{j0.3661}$ ,  $T_i = 1$ )

Angles	Ang 1	Ang 2	Ang 3	Ang 4
$\alpha_i$	-0.091534	-0.876933	-1.662331	-2.447729
Initial angles $\alpha_i^{(0)}$	-0.091534	-0.876933	-1.662331	-2.447729
Converged angles $\alpha_i^{(T_i)}$	-0.091549	-0.876707	-1.662340	-2.447756
Selected angles	√	√	√	√

Table 2  
Angles calculated for the first object in Fig. 3(a) ( $GC_{P,Q} = GC_{0,4} = 0.1134e^{j2.3264}$ ,  $T_i = 31$ )

Angles	Ang 1	Ang 2	Ang 3	Ang 4
$\alpha_i$	-0.581608	-1.367006	-2.152404	-2.937803
Initial angles $\alpha_i^{(0)}$	-0.581608	-1.367006	-1.152404	-2.937803
Converged angles $\alpha_i^{(T_i)}$	-0.575485	-1.361188	-2.147461	-2.932106
Selected angles	√	√	√	√

Table 3

Angles calculated for the second object in Fig. 2(b) ( $GC_{P,Q} = GC_{0,4} = 0.3471e^{j1.9672}$ ,  $T_i = 54$ )

Angles	Ang 1	Ang 2	Ang 3	Ang 4
$\alpha_i$	-0.491806	-1.277204	-2.062603	-2.848001
Initial angles $\alpha_i^{(0)}$	-0.491806	-1.277204	-2.062603	-2.848001
Converged angles $\alpha_i^{(T_i)}$	-0.685285	-1.278643	-2.160790	-2.837659
Selected angles				√

Table 4

Angles calculated for the second noisy object in Fig. 3(b) ( $GC_{P,Q} = GC_{0,4} = 0.2146e^{j0.2837}$ ,  $T_i = 102$ )

Angles	Ang 1	Ang 2	Ang 3	Ang 4
$\alpha_i$	-0.070927	-0.856325	-1.641723	-2.427121
Initial angles $\alpha_i^{(0)}$	-0.070927	-0.856325	-1.641723	-2.427121
Converged angles $\alpha_i^{(T_i)}$	-0.162134	-0.848648	-1.511753	-2.434725
Selected angles		√		

all the four angles satisfying these two constraints. The corresponding reflection-symmetric axes are shown in Fig. 2(a2) at angles  $-\alpha_i^{(T_i)}$ ,  $i = 1, 2, 3, 4$ .

The table and figures corresponding to the noisy version of this object are, respectively, shown in Table 2 and Fig. 5. We find the curves in Fig. 5(b) are similar to that in Fig. 4(b), although their 1D radial projection functions, respectively, in Fig. 5(a) and (b) are slightly different due to noise.

*Experiments on the second image object shown in Figs. 2(b) and 3(b).* Among the  $N = 15$  GC moments, the magnitude of  $GC_{0,4}$  is the largest one (Fig. 2(b)). The reflection-symmetric axes as determined by only  $GC_{0,4}$  is shown in Fig. 2(b1). Table 3 shows the corresponding angles  $\alpha_i$ , the initial angles  $\alpha_i^{(0)}$ , and the converged angles  $\alpha_i^{(T_i)}$ . Here  $i = 0, 1, \dots, 3$ . In Fig. 6(b), the grey curve represents the term  $E' = 2\pi(R_{0,4} \sin(\varphi_{0,4} + 4\alpha))^2$ . Fifty-four iterations were used to obtain all four local minima. Fig. 6(b) visually shows that *three out of the four* converged angles cannot be the true reflection axes, since their corresponding  $E_{Asym}^{\alpha_i}$  are too large and hence failed to meet our first constraint. Fig. 2(b2) therefore shows a single reflection-symmetric axis with the angle  $-0.304$  detected for this object. Table 4 and Fig. 7, respectively, show the angles and curves corresponding to the noisy version of this object, while the unique reflection-symmetric axis detected is shown as a grey line in Fig. 3(b2).

*Experiments on the third image object shown in Figs. 2(c) and 3(c).* For this object (Fig. 2(c)), the magnitude of  $GC_{0,3}$

is the largest one. The reflection-symmetric axes as determined by  $GC_{0,3}$  are shown in Fig. 2(c1), all of which are actually the *false* axes. The corresponding angles  $\alpha_i$ , the initial angles  $\alpha_i^{(0)} = \alpha_i$ , and the converged angles  $\alpha_i^{(T_i)}$  are shown in Table 5. Here  $i = 0, 1, 2$ . In Fig. 8(b), the grey curve represents the term  $E' = 2\pi(R_{0,3} \sin(\varphi_{0,3} + 3\alpha))^2$ . Twenty-nine iterations were used to obtain all three local minima. The Fig. 8(b) visually shows that none of these angles can be the true reflection axes, since both their  $E_{Asym}^{\alpha_i}$  and  $\|\alpha_i^{(T_i)} - \alpha_i^{(0)}\|$  are too large, hence failed to satisfy our two constraints. So in Fig. 2(c2), no reflection-symmetric axis is detected. The table and figures corresponding to the noisy version of this object are, respectively, shown in Table 6 and Fig. 9. Again, no reflection-symmetric axis is detected in Fig. 3(c2).

*Experiments on the fourth image object shown in Figs. 2(d) and 3(d).* The object in Figs. 2(d) and 3(d) is not perfectly reflection-symmetric. Among 15 GC moments, the magnitude of  $GC_{0,6}$  is the largest one. The reflection-symmetric axes as determined by  $GC_{0,6}$  are shown in Fig. 2(d1). Table 7 shows the corresponding angles  $\alpha_i$ , the initial angles  $\alpha_i^{(0)} = \alpha_i$ , and the converged angles  $\alpha_i^{(T_i)}$ . Here  $i = 0, 1, \dots, 5$ . In Fig. 10(b), the grey curve represents the term  $E' = 2\pi(R_{0,6} \sin(\varphi_{0,6} + 6\alpha))^2$ . A total of 125 iterations were used to get six local minima. Fig. 10(b) visually indicates that *three of the six* converged angles cannot be the reflection axes, since both their  $E_{Asym}^{\alpha_i}$  and  $\|\alpha_i^{(T_i)} - \alpha_i^{(0)}\|$  are too large. Fig. 2(d2) shows the three detected

Table 5

Angles calculated for the third object in Fig. 2(c) ( $GC_{P,Q} = GC_{0,3} = 0.3515e^{-0.4857j}$ ,  $T_i = 29$ )

Angles	Ang 1	Ang 2	Ang 3
$\alpha_i$	0.161922	-0.885275	-1.932473
Initial angles $\alpha_i^{(0)}$	0.161922	-0.885275	-1.932473
Converged angles $\alpha_i^{(T_i)}$	0.236182	-0.812450	-1.858345
Selected angles			

Table 6

Angles calculated for the third noisy object in Fig. 3(c) ( $GC_{P,Q} = GC_{0,3} = 0.2146e^{-1.6584j}$ ,  $T_i = 63$ )

Angles	Ang 1	Ang 2	Ang 3
$\alpha_i$	0.552828	-0.494369	-1.541567
Initial angles $\alpha_i^{(0)}$	0.552828	-0.494369	-1.541567
Converged angles $\alpha_i^{(T_i)}$	0.618715	-0.428860	-1.477560
Selected angles			

Table 7

Angles calculated for the fourth object in Fig. 2(d) ( $GC_{P,Q} = GC_{0,6} = 0.1160e^{-1.7396j}$ ,  $T_i = 125$ )

Angles	Ang 1	Ang 2	Ang 3	Ang 4	Ang 5	Ang 6
$\alpha_i$	0.289932	-0.233666	-0.757265	-1.280864	1.804463	-2.328061
Initial angles $\alpha_i^{(0)}$	0.289932	-0.233666	-0.757265	-1.280864	1.804463	-2.328061
Converged angles $\alpha_i^{(T)}$	0.189188	-0.228597	-0.858651	-1.274022	-1.905801	-2.321693
Selected angles		√		√		√

Table 8

Angles calculated for the fourth noisy object in Fig. 3(d) ( $GC_{P,Q} = GC_{0,6} = 0.0755e^{-0.7626j}$ ,  $T_i = 256$ )

Angles	Ang 1	Ang 2	Ang 3	Ang 4	Ang 5	Ang 6
$\alpha_i$	0.127101	-0.396497	-0.920096	-1.443695	-1.967294	-2.490892
Initial angles $\alpha_i^{(0)}$	0.127101	-0.396497	-0.920096	-1.443695	-1.967294	-2.490892
Converged angles $\alpha_i^{(T)}$	0.044609	-0.391255	-1.004037	-1.438848	-2.055637	-2.484633
Selected angles		√		√		√

reflection-symmetric axes. Table 8 and Fig. 11, respectively, show the angles and curves corresponding to the noisy version of this object. Also, three reflection-symmetric axes were accurately detected in Fig. 3(d2).

#### 4.2. Real objects

In the above experiments, the test images are actually grey-level images. However, they are seemingly binary due to their grey-level values being close to black and white. Notice that our method is suitable to detecting reflectional symmetries of the grey-level images, and even

real images of real objects. Fig. 12(a) shows an example, which is a slice image of a human brain.

The robustness of our method against random noises is dependent on that of GC moments against noises. In Ref. [10] it has been shown that GC moments are robust to Gaussian noise. Fig. 12(b)–(e) shows four noisy images that were corrupted by Gaussian noise with standard deviation of 15, 30, 45, 60, respectively. The solid lines in Fig. 12 denote the reflection-symmetric axes of the corresponding images. Table 9 gives the deviation values (degrees) between the orientations of reflection-symmetric axes of noisy images (Fig. 12(b)–(e)) and the orientation of

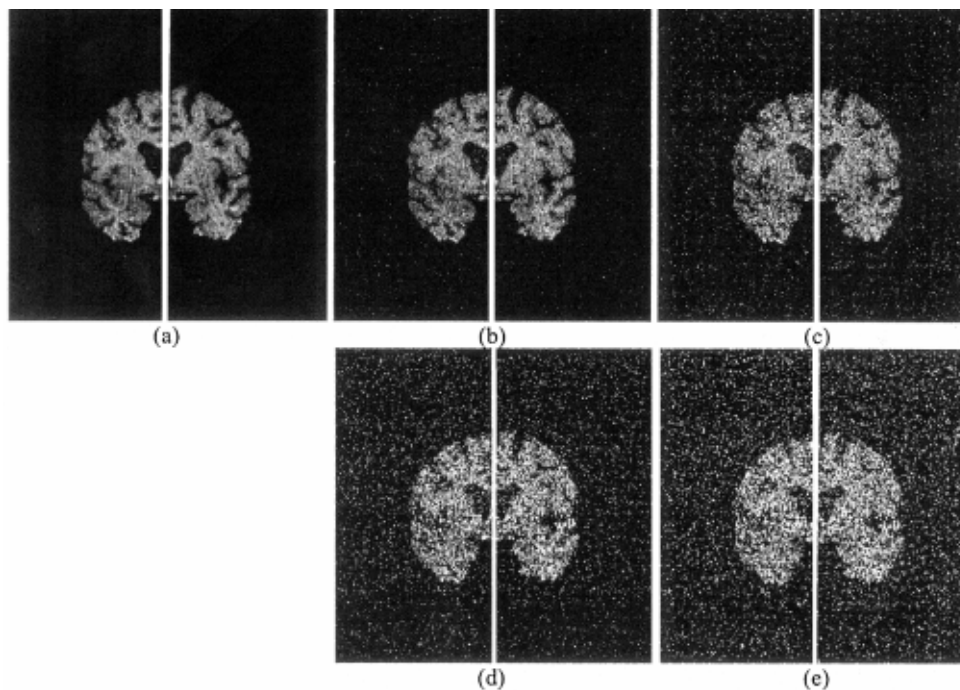


Fig. 12. Reflection symmetries detection on the image of the real object, human brain: (a) noise-free image; (b)–(e) noisy images that were corrupted by Gaussian noise with standard deviation of 15, 30, 45, 60, respectively.

Table 9

The deviation value of the symmetric orientation with the increase of standard deviation of Gaussian noise

Standard deviation of Gaussian noise variance	15	30	45	60
Deviation values (degree)	0.28	-0.85	-0.80	-0.75

Table 10

The deviation value (degree) of the symmetric orientation due to the deviation of the detected image centre from the real image centre (dx, dy)

(dx, dy)	-6	-4	-2	0	2	4	6
-6	-5.4	-3.1	-1.8	-0.2	1.1	2.8	4.4
-4	-4.8	-3.0	-1.6	-0.3	1.2	2.8	4.2
-2	-4.3	-2.4	-1.5	-0.2	1.3	3.0	4.7
0	-4.0	-2.3	-1.5	0	1.4	2.6	3.8
2	-4.1	-2.5	-1.5	0.1	1.3	2.5	3.8
4	-4.2	-3.0	-1.6	-0.2	1.4	2.9	4.0
6	-4.8	-3.5	-2.0	-0.4	1.1	2.7	4.2

reflection-symmetric axis of noise-free image (Fig. 12(a)). It is easy to observe that the deviations are very small.

#### 4.3. Sensitivity to the errors of locating image centre

Most symmetric detection methods, including our method, rely on the assumption that the geometric centres of the mass of the objects are known. While there exist several techniques for locating their centre of mass, none are completely accurate. In this section, we evaluate the sensitivity of our method to the errors of locating the centre of the image. Suppose that the detected image centre deviates from the real image centre, at dx in the  $x$  dimension and dy in the  $y$  dimension. For the image  $256 \times 256$  in Fig. 12(a), Table 10 shows the deviation value (*degree*) of the symmetric orientation due to the deviation of the detected image centre from the real image centre, (dx, dy). The biggest orientation deviation is  $-5.4^\circ$  when (dx, dy) is equal to  $(-6, -6)$ . Basically, this amount of deviation is acceptable. Therefore, our method is relatively robust to the error of locating image centre.

## 5. Conclusions

In this paper, the problem of detecting reflectional symmetries has been formulated as a process of calculating the local minima of the asymmetric energy term, which

corresponds to the asymmetric component of the studied object. The asymmetric energy term is defined by a set of GC moments of the object. The local minima of this energy term are computed by using a steepest descent technique, whose initialisation is obtained by a dominant GC moment with the largest magnitude. Two constraints are proposed to determine whether the angles corresponding to the local minima of the asymmetric energy term are the negative angles of the actual reflection-symmetric axes. Furthermore, our method is able to detect visually symmetric objects. Typical images of logos and real objects are also used to demonstrate the performance of our method.

## References

- [1] W.G. Oh, M. Asada, S. Tsuji, Model-based matching using skewed symmetry information, in: Proceedings of the International Conference on Pattern Recognition, 1988, pp. 1043–1045.
- [2] G. Marola, Using symmetry for detecting and locating objects in a picture, *Computer Vision Graphics and Image Processing* 46 (1989) 179–195.
- [3] F. Labonte, Y. Shapira, P. Cohen, A perceptually plausible model for global symmetry detection, in: Proceedings of the Fourth International Conference on Computer Vision, 1993, pp. 258–263.
- [4] T. Zielke, M. Brauckmann, W.V. Seelen, Intensity and edge-based symmetry detection with an application to car-following, *Computer Vision, Graphics, and Image Processing: Image Understanding* (1993) 58 (2) 177–190.
- [5] M. Atallah, On symmetry detection, *IEEE Transactions on Computers* 34 (7) (1985) 663–666.
- [6] G. Marola, On the detection of the axes of symmetry of symmetric and almost symmetric planar images, *IEEE Transactions on Pattern Analysis and Machine Intelligence* 11 (1) (1989) 104–108.
- [7] T. Masuda, K. Yamamoto, H. Yamada, Detection of partial symmetry using correlation with rotated-reflected images, *Pattern Recognition* 26 (8) (1993) 1245–1253.
- [8] C. Sun, J. Sherrah, 3D symmetry detection using the extended Gaussian image, *IEEE Transactions on Pattern Analysis and Machine Intelligence* 19 (2) (1997) 164–168.
- [9] L. Oriat, E. Lantz, Subpixel detection of the center of an object using a spectral phase algorithm on the image, *Pattern Recognition* 31 (6) (1998) 761–771.
- [10] D. Shen, H.H.S. Ip, Generalized affine invariant image normalization, *IEEE Transactions on Pattern Analysis and Machine Intelligence* 19 (5) (1997) 431–440.
- [11] D. Shen, H.H.S. Ip, Optimal axes for defining the orientations of shapes, *IEE Electronic Letters* 32 (20) (1996) 1873–1874.
- [12] D. Shen, H.H.S. Ip, K.K.T. Cheung, E.K. Teoh, Symmetry detection by generalized complex (GC) moments: a close-form solution, *IEEE Transactions on Pattern Analysis and Machine Intelligence* 21 (5) (1999) 466–476.